CrossMark

ORIGINAL PAPER

Lignite-derived mesoporous N- and O-enriched carbon sheet: a low-cost promising electrode for high-performance electrochemical capacitors

Siqi Zhu[1] · Qiuli Chen[1] · Yaoyao Shi[1] · Zhiyi Chen[1] · Ruiqi Bao[1] · Lu Zhou[1] ·
Linrui Hou[1] · Kwun Nam Hui[2] · Changzhou Yuan[1,2]

Abstract In the work, we successfully fabricate mesoporous N- and O-enriched carbon (NOC) with adjustable porosity and specific surface area (SSA) by using low-cost lignite as a precursor coupled with general KOH or $ZnCl_2$ activation for electrochemical capacitors (ECs). Physicochemical and electrochemical characterizations reveal that chemical activating agents influence significantly upon the specific morphology, pore structure, and electrochemical performance of the resultant products. Strikingly, KOH-activated NOC (NOC-K) sheets are endowed with high SSA of ~1257 m^2 g^{-1}, large pore volume of 1.3 cm^3 g^{-1}, and optimized pore size of ~3 nm, rendering its electrochemical capacitance superior to those of NOC and $ZnCl_2$-activated NOC (NOC-Z) in 6 M KOH. Thanks to its rich mesoporosity coupled with large electroactive SSA and heteroatom doping (N of ~4.8 at.% and O of ~23.3 at.%) effect, the NOC-K electrode yields even better electrochemical behaviors in 1 M H_2SO_4 than those in 6 M KOH.

Abbreviations

NOC	N- and O-enriched carbon
SSA	Specific surface area
SED	Specific energy density
ECs	Electrochemical capacitors
NOC-Z	$ZnCl_2$-activated NOC
NOC-K	KOH-activated NOC
CE	Coulombic efficiency
EDLCs	Electrochemical double-layer capacitors
SC	Specific capacitance
BET	Brunauer–Emmett–Teller
RT	Room temperature
FESEM	Field-emission scanning electron microscope
TEM	Transmission electron microscope
HRTEM	High-resolution transmission electron microscope
PSD	Pore size distribution
BJH	Barrett–Joyner–Halenda
XPS	X-ray photoelectron spectroscopy
CV	Cyclic voltammetry
CP	Chronopotentiometry
EIS	Electrochemical impedance spectroscopy
SCE	Saturated calomel electrode
SL	Shengli
SPD	Specific power density
BE	Binding energy

✉ Linrui Hou
  houlr629@163.com

✉ Kwun Nam Hui
  bizhui@umac.mo

✉ Changzhou Yuan
  ayuancz@163.com

[1] School of Materials Science & Engineering, Anhui University of Technology, Ma'anshan 243002, Peoples Republic of China

[2] Institute of Applied Physics and Materials Engineering, Faculty of Science and Technology, University of Macau, Macau, Peoples Republic of China

Introduction

In recent years, electrochemical double-layer capacitors (EDLCs), as a promising high-power energy source, have

attracted tremendous attentions for versatile applications where high power density, high Coulombic efficiency (CE), and long-term cycling life are urgently required. In general, the energy storage mechanism of EDLCs primarily involves charge storage at the electrode/electrolyte interfaces through reversible ion adsorption/desorption, thus charging the so-called double-layer capacitance [1–4]. In this term, the real specific capacitance (SC) of one electrode should depend greatly upon its efficient specific surface area (SSA), that is, the double-layer capacitance would be directly proportional to electroacitve surface freely accessible to the electrolyte ions [1–4], rather than the SSA measured by the Brunauer–Emmett–Teller (BET) method. It is therefore necessary yet urgent to explore several efficient strategies to increase the effective SSA of electrodes for maximizing their specific energy density (SED).

Among various available electrode candidates for EDLCs, porous carbons have been investigated intensively so far, benefiting from their well-developed porous structure, good electronic conductivity, controllable surface property, excellent physicochemical stability as well as cost efficiency and accessibility [1–7]. Unfortunately, carbon materials are typically featured by the inert surface, rendering electrolyte ions difficult to penetrate into the inner surface of carbon framework for efficient charge storage. It is for this reason that some functional groups and/or heteroatoms (such as N and O) are highly expected to introduce into porous carbon scaffolding with ultimate aim to enhance the electrode/electrolyte wettability via the formation of polar functional groups [6, 8–11]. Besides this, the introduced N and O species further provide the acid/base properties to the carbon, contributing the extra pseudo-capacitance, i.e., additional Faradaic effects, from the striking redox process of the heteroatom functionalities [6, 11–13]. One also should note that the heteroatom N is a more promising candidate, owing to its small atomic diameter, high electronegativity, and additional free electrons [7, 12–14], which make the N-doped carbon a better electronic conductor. In addition, the suitable pore structure of carbon materials plays another significant role in maximizing their electrochemical capacitance. Recent reports [15–17] suggest that appropriate pore sizes (2–5 nm) of the porous electrode are critical to ease the mass transfer of electrolyte within these pores for double-layer charging/discharging and fast redox reactions. Therefore, the N- and O-enriched carbon (NOC) with suitable mesoporosity would be an excellent electrode for advanced electrochemical capacitors (ECs), where the advantages of indefinitely reversible double-layer capacitance and rapid reversible pseudo-capacitance are smartly combined together.

As regards to EDLCs, material cost, as a limiting factor for their practical applications, restricts the utilization of complicated synthesis and expensive precursors. With the scalably cost-effective fabrication of high-performance NOC in mind,

we thus believe that it is of great significance to explore the cheap precursors or universal resources in nature, such as human hairs [13], dead leaves [18], animal bones [19], fish scale [20], banana fibers [21], rice husk [22], cashmere [23], and sulfonated pitch [24], for simple synthesis of mesoporous NOC. Furthermore, the NOC can be prepared by directly pyrolyzing what are naturally rich in N and O elements, strongly favoring for more homogeneous incorporation of the N and/or O species into the bulk carbon, rather than just on their surfaces [25]. Abundant reserves and cost-effective availability of coals, especially lignite [26, 27], further stimulate their utilization to produce higher value-added products for broader applications. It is well known that lignite, as a low-rank coal, is mainly used as fuel for power plant but with some disadvantages including low calorific value and high mineral matter and moisture contents. Therefore, it would be better to further explore its non-fuel application. Appealingly, note that the lignite commonly possesses a relatively high proportion of N-containing organic species, such as humin and humic acids [26, 27]. As a result, one appealing way is probably the elegant utilization of the lignite as raw sources to synthesize high-performance NOC for ECs.

With comprehensive considerations above, in the work, we controllably synthesized mesoporous NOC products by using the lignite as a starting precursor coupled with facile KOH or ZnCl$_2$ activation. Great influences of activating agents upon the specific morphology, pore structure, and corresponding electrochemical performance of the resultant NOC samples were systematically investigated. The KOH-activated NOC (denoted as NOC-K) sheets with the largest SSA and appropriate pore size yielded even better electrochemical capacitance than those for NOC and ZnCl$_2$-activated NOC (designed as NOC-Z) electrodes in 6 M KOH. Remarkably, the NOC-K delivered much better electrochemical properties, compared to those in 6 M KOH, thanks to the optimal mesoporosity, large electroactive SSA, and desirable heteroatom doping effects. A NOC-K-based symmetric device obtained a large SED of ~6.7 Wh kg^{-1} in 1 M H$_2$SO$_4$. The excellent supercapacitive performance encourages its aspired commercial exploitation for ECs.

Experimental

Synthesis and characterization of the NOC, NOC-Z, and NOC-K products

The lignite from Shengli (SL) mine (China) was used as the carbon precursor. The proximate and ultimate analyses (Table S1, see Supporting Information) of the SL lignite were first performed. After being washed, dried, pulverized, and sieved, the as-obtained black granular sample of 150–250 μm in size was then stored in an airtight container before

use. After being carbonized in a tubular furnace at a temperature of 500 °C for 2 h with a heating rate of 5 °C min^{-1} under N$_2$ atmosphere, the "crude" (unactivated) NOC product was then prepared. During the following KOH-activated process, the as-obtained NOC was homogeneously mixed with activation agent of KOH in a KOH/NOC ratio of 3:1 (W/W). Afterwards, the mixture was further activated under N$_2$ flow at 800 °C for 2 h in a tubular furnace with a heating rate of 3 °C min^{-1}. After cooled to room temperature (RT), the resultant material was first washed with the mixed HF–HCl solution, rinsed with copious distilled water until neutral, and then dried in vacuum at 100 °C. The NOC-K sample was finally prepared. For comparison, the ZnCl$_2$-activated process was also carried out. At RT, 0.5 g of the given NOC was impregnated with aqueous ZnCl$_2$ solution (3 M) for 12 h. After being separated by filtration, and dried at 80 °C overnight under vacuum, the product was further activated in a quartz tube at 800 °C for 2 h with a heating rate of 3 °C min^{-1}. The powder was further washed with mixed HF–HCl solution and copious water in sequence and dried at 120 °C. The NOC-Z was prepared.

Ultimate analyses of the carbon precursor were conducted on an elemental analyzer (Vario EL III, Elementar, Germany). The powder X-ray diffraction (Max 18 XCE, Japan) pattern from 20° to 80° was measured by using a Cu Ka source ($\lambda = 0.154056$ nm) at a scanning speed of 3° min^{-1}. The morphologies and micro-structures of the resulting samples were examined by field-emission scanning electron microscopy (FESEM, JEOL-6300F, 15 kV), transmission electron microscope (TEM), and high-resolution transmission electron microscope (HRTEM) of JEOL JEM 2100 system at an acceleration voltage of 200 kV. N$_2$ adsorption/desorption was determined by BET measurement using an ASAP-2020 surface area analyzer. The pore size distribution (PSD) was derived from the adsorption branch of the Barrett–Joyner–Halenda (BJH) method. X-ray photoelectron spectroscopy (XPS) measurements were performed on a PHi5000 X-ray photoelectron spectrometer with an Al Ka excitation source (1486.6 eV). The spectra were fitted with the XPSPEAK41 software. Before XPS analysis, the samples were dried at 120 °C in a vacuum oven overnight to remove the absorbed water. The Raman analysis of the sample was recorded by laser Raman (T6400, Jobion yzon crop. France). Electronic conductivity was performed by a four-point probe meter (SDY-5, Guangzhou, China) at RT.

Electrochemical tests

The working electrode was prepared with the electroactive NOC-K (NOC or NOC-Z), acetylene black, and polytetrafluoroethylene in a weight ratio of 8:1.5:0.5. A small amount of distilled water was then added to make more homogeneous mixture, which was pressed onto Ni foam (1 cm^2)

at a pressure of 15 MPa for following electrochemical tests by cyclic voltammetry (CV), chronopotentiometry (CP), and electrochemical impedance spectroscopy (EIS) measurements performed with an IVIUM electrochemical workstation (the Netherlands). EIS tests were carried out in 6 M KOH with a frequency loop from 10^5 to 0.01 Hz using a perturbation amplitude of 5 mV at −0.4 V (vs. a saturated calomel electrode (SCE)). The mixture was also smeared onto the pretreated graphite substrate (1 cm^2) [28] instead of electrochemical characterizations in 1 M H$_2$SO$_4$. All experiments were carried out in three-electrode cells with a platinum plate counter electrode (1 cm^2) and a SCE reference electrode at RT. The electrolyte used here was 6 M KOH (or 1 M H$_2$SO$_4$) aqueous solution. The typical loading of the NOC-K (NOC-Z or NOC) is 5 mg cm^{-2} for electrochemical tests in acidic/basic electrolytes. Cycling performance was carried out with a CT2001D tester (Wuhan, China). Furthermore, a symmetric device was fabricated by using two NOC-K electrodes face to face in 1 M H$_2$SO$_4$ (or 6 M KOH) solution. The SCs of the electrode or symmetric devices with 6 M KOH or 1 M H$_2$SO$_4$ can be calculated by using the following equation:

$$SC = \frac{It}{\Delta V} \tag{1}$$

where I, t, and ΔV denote discharge current (A g^{-1}), discharging time (s), and discharge potential interval (V), respectively. And the SED and specific power density (SPD) of the NCC-K-based symmetric ECs can be calculated using the following equation:

$$SED = SPDt = \frac{1}{2} SC(\Delta V)^2 \tag{2}$$

where SC is the capacitance of the symmetric ECs, which is calculated based on the whole mass of the two electrodes in symmetric devices.

Results and discussion

Physicochemical characterization

In order to well develop appropriate pore network in carboneous materials, physical and/or chemical activation is generally required [29, 30]. Compared to physical activation, chemical strategy, where KOH, ZnCl$_2$, and K$_2$CO$_3$ are commonly used, has lots of distinct advantages including lower activation temperature, higher yield, shorter activation time, and so on [30]. In the synthetic methodology developed here, two procedures, involving in the pre-carbonization and subsequent chemical activation, were carried out for controllable synthesis of hierarchical porous NOC products. The dried lignite was first pre-carbonized at 500 °C to produce NOC

samples. Then, the resultant NOC was mixed homogeneously with KOH or $ZnCl_2$ and further activated at 800 °C to effectively develop the rich mesoporosity of the final products.

Obviously, the typical XRD pattern (Fig. S1, see Supporting Information) of the as-fabricated NOC-K exhibits two characteristic peaks located at around $2\theta = 26.2°$ corresponding to the (002) and 44.3° related to the (101) planes, and the representative FESEM image of the resulting NOC-K is demonstrated in Fig. 1a. Obviously, the NOC-K sample presents irregular sheet-like morphology, while its analogue NOC-Z is morphologically monolithic with ordinary particulate structure (Fig. S2, see Supporting Information). TEM measurements were further performed to elucidate the microstructure of the resulting NOC-K more clearly. As observed in Fig. 1b–e, sheet-like structure of the NOC-K is clearly presented, and the brighter contrast in these TEM images reveals the extremely porous nature of the NOC-K itself. HRTEM image (Fig. 1f), detected from a sampling area indicated by the red rectangle region in Fig. 1d, further verifies that the unique NOC-K sheets are really a structurally porous architecture in the nano-scale and/or sub-nanometer range. This prominent porous feature would contribute to much more electroactive sites and provide more convenient mass transport meantime for efficient charge storage. As discussed above, different activating agents result in distinct morphologies, which should be rationally ascribed to different

activation mechanisms of KOH and $ZnCl_2$. As for the KOH activation, etching the carbon framework between various potassium compounds with carbon and the formation of H_2O and CO_2 in the activation system positively contribute to the generation of well-developed pore network in the resultant product [31, 32]. Furthermore, the metallic K formed during the activation can efficiently intercalate into the carbon lattices of the carbon matrix, leading to the expansion of the carbon lattices [31, 33]. After removal of the intercalated metallic K and/or K-based compounds by following washing, the expanded carbon lattices cannot return to their previous structure, and thus, the NOC-K sheets with rich porosity that are necessary for large SSA are created meanwhile. With regard to the $ZnCl_2$ activation process, it is generally known that $ZnCl_2$ just acts as a dehydration agent [34, 35]. Molina-Sabio and Rodríguez-Reinoso [34] once pointed out that the impregnation with $ZnCl_2$ first resulted in degradation of the cellulosic material, and on carbonization, produced dehydration that led to charring and aromatization of the carbon skeleton, and creation of the pore structure [34, 35]. Thus, irregular NOC-Z particles are obtained.

N_2 sorption isotherm measurements were comparatively probed at a temperature of 77 K to investigate the development of porosity and BET SSA with the chemical activation. As plotted in Fig. 2a, the isotherm of the NOC sample should be classified as type IV with a distinct H3-type hysteresis loop at a relative high pressure range, according to the IUPAC classification, indicating typical mesoporous characteristics of the NOC, which can be further confirmed by its PSD data obtained by the BJH method (Fig. 2b). Similar to those for NOC, just mesoporous characteristics can be observed for the NOC-Z product, as depicted in Fig. 2c, d. As a contrast, the N_2 desorption/adsorption isotherm of the NOC-K is close to a combination form of type I and type IV, as demonstrated in Fig. 2e, suggesting the co-existence of micropores and mesopores, which is evidently supported by its PSD (Fig. 2f). As examined from texture parameters of the three (Table S2, see Supporting Information), the NOC just possesses low BET SSA of ~19 $m^2\ g^{-1}$, small pore volume of ~0.034 $cm^3\ g^{-1}$ as well as large pore size of ~20.9 nm. After $ZnCl_2$ activation process, one should note that the NOC-Z demonstrates higher SSA of 829 $m^2\ g^{-1}$ and larger pore volume (1.3 $cm^3\ g^{-1}$) along with a smaller pore size of ~7.6 nm. Encouragingly, the SSA and pore volume of the NOC-K dramatically increase up to ~1257 $m^2\ g^{-1}$ and ~1.3 $cm^3\ g^{-1}$, respectively, and the average pore size is greatly down to ~3 nm, which is evidently located in the optimal pore size range of 2–5 nm, as reported before [15–17, 36]. Considering the comparative data above, it is easy to conclude that KOH is more effective to produce carbons with large SSA and appropriate mesopore size for efficient charge storage. Thus, we expect that the NOC-K with the largest SSA and optimized pore size would be
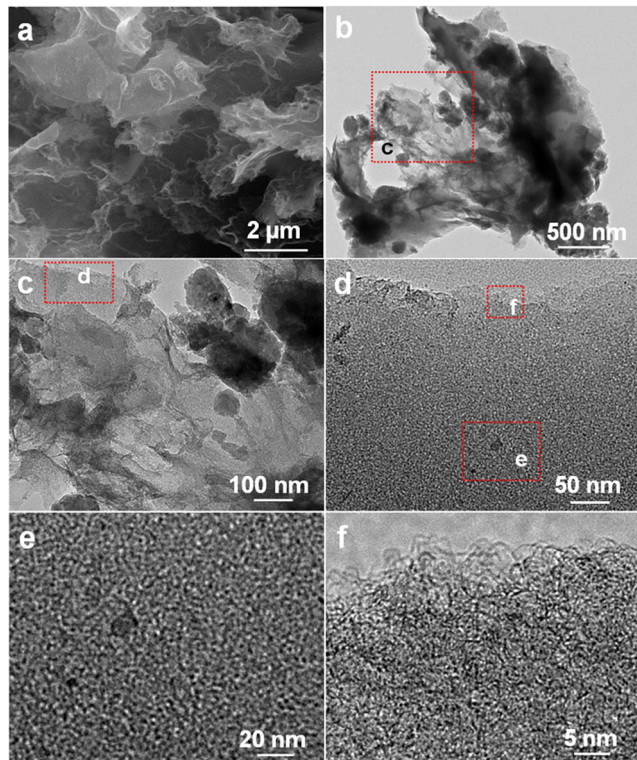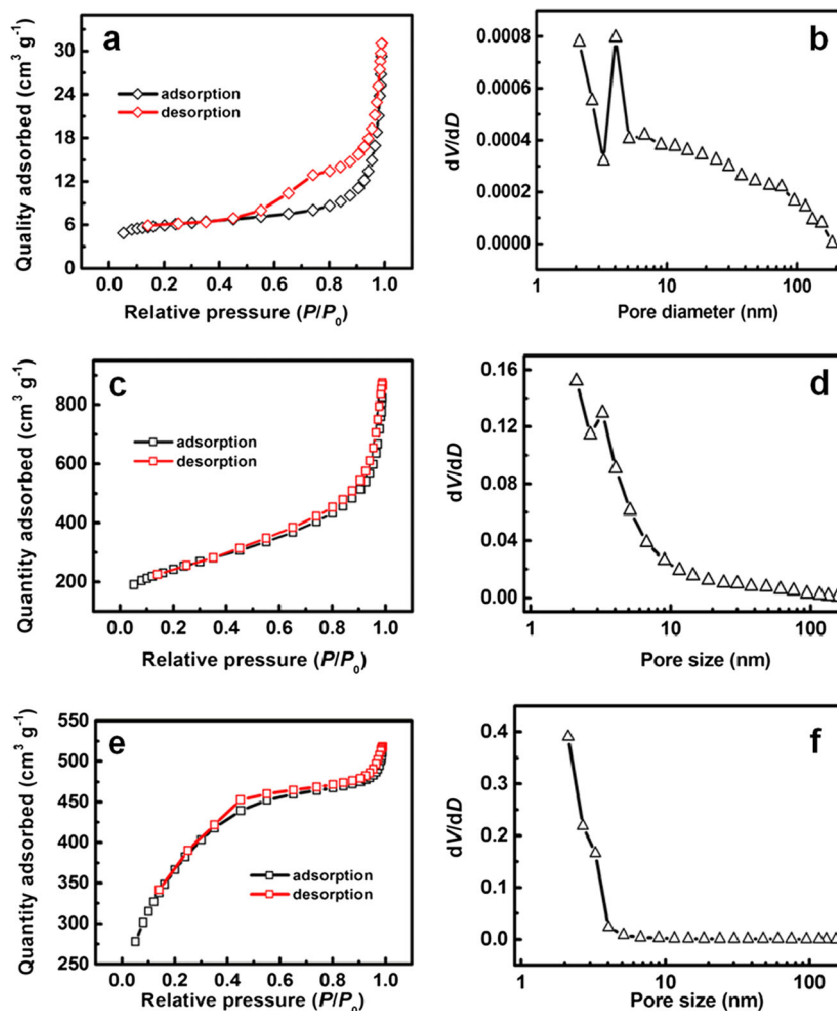

Fig. 1 FESEM (**a**), TEM (**b–e**), and HRTEM (**f**) images of the sample. The images in **c–f** are the magnified ones of the red *rectangle regions* in panels **b**, **c**, and **d**, respectively

Fig. 2 Nitrogen adsorption/ desorption isotherm and pore size distribution of the NOC (**a**, **b**), NOC-Z (**c**, **d**), and NOC-K (**e**, **f**)

the most promising electroactive material among the three for advanced ECs.

To further study the graphitization degree and electronic conductivity of the NOC-K sample, Raman spectrum and corresponding fitted data is shown in Fig. 3. Obviously, the spectrum shows two characteristic peaks located at ~1590 and ~1317 cm^{-1}. The former centered at ~1590 cm^{-1} (i.e., G
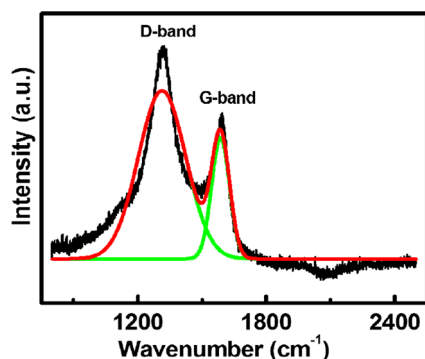

Fig. 3 Raman spectrum and corresponding fitted data of the as-fabricated NOC-K sample

(graphitic)-band) is commonly attributed to the vibration of sp^2-bonded carbon atoms in two-dimensional hexagonal lattice [37], and the latter, i.e., D (defects and disorder)-band, is associated to the defects and disorders of structures in carbon materials. The stronger D-band should be partially ascribed to somewhat disorder caused by the incorporation of heteroatom N and O in the NOC-K framework. The ratio of "D-band" to "G-band", also known as the "*R* value," reveals the amount of structurally ordered graphite crystallites and reflects its graphitization degree. The *R* value of the NOC-K is calculated as ~1.1, less than that (~1.23) of the human hair-derived carbon at the same temperature [13], suggesting high structural alignment of the NOC-K, which should be responsible well for its desirable electronic conductivity of ~21 S cm^{-1}.

The surface chemistry of the carbon plays a significant role in enhancing its electrochemical capacitance, as established previously [6–11, 13]. Typical TEM elemental mapping and composition analysis (Fig. S3, see Supporting Information) of the NOC-K sheets confirms the presence and homogeneous distribution of the C, N, and O within the sample. The nature of the three species was nextly investigated by XPS

measurement. Corresponding XPS spectra and fitted plots are demonstrated entirely in Fig. 4a–d. The survey spectrum (Fig. 4a) shows the presence of C, O, and N in the NOC-K, and the contributions of each species obtained by fitting the C 1s, N 1s, and O 1s core level spectra are collected and compiled exhaustively in Table 1, as well as peak positions and relative concentrations. The atomic contents of C, O, and N elements are quantitatively calculated as ~72.0, ~23.2, and ~4.8 at.%, respectively. Typical C 1s spectrum (Fig. 4b) can be deconvoluted into the following five bands: C in rings (sp^2 C=C) without N at a binding energy (BE) of 284.6 eV (C-I, ~64.7 at.%); sp^3 C–C at 285.2 eV (C-II, ~9.6 at.%); C–C singly bound to O in phenol and ether (i.e., C*–OH, or C*–O–*C) and C*–N groups at 286.1 eV (C-III, ~8.4 at.%); C sp^2 linked to N (i.e., C*=N) and O (i.e., C*=O or O–C*–O) groups around at 287.3 eV (C-IV, ~5.6 at.%); and C in carbonate groups and/or adsorbed CO and CO_2 at 289.2 eV (C-V, ~11.7 at.%) [37–39]. In the region of N 1s core level spectrum (Fig. 4c), the chemical states of the N atom with BEs of 398.7 and 399.5 eV can be identified as the pyridinic N (N-I, ~13.7 at.%) and N-pyrrolic/N-pyridonic (N-II, ~86.3 at.%), respectively, by using a Gaussian fitting method [40, 41]. Two characteristic peaks at 531.3 and 533.3 eV in the O 1s spectrum (Fig. 4d) can be related to the O in the quinine-type group (O*=C) (O-I, ~91.1 at.%), and non-carbonyl (ether-type) oxygen atoms (O-II, ~8.9 at.%) in esters and anhydrides bound to the NOC-K surface [12]. As established well [11], the pseudo-capacitive interactions just can take place on negatively charged N-I and N-II and the "O*=C" group (O-I) (Fig. S4, see Supporting Information) [11, 42]. With the systematic XPS investigation above, it is easy to conclude that the

Table 1 XPS peak positions and relative content of C, O, and N species in the as-obtained NOC-K sample. Estimation of the heteroatom species fraction is based on the area of their respective peaks

	Peak position (eV)	at.%
C species (72 at.%)		
C-I	284.6	64.7
C-II	285.2	9.6
C-III	286.1	8.4
C-IV	287.3	5.6
C-V	289.2	11.7
O species (23.2 at.%)		
O-I	531.3	8.9
O-II	533.3	91.1
N species (4.8 at.%)		
N-I	398.7	13.7
N-II	399.5	86.3

NOC-K possesses high-content N-pyrrolic/N-pyridonic (N-II, ~4.1 at.%) and quinine-type group (O* = C) (O-I, ~21.1 at.%) with remarkable pseudo-capacitive contributions, which significantly favors to improve the final electrochemical capacitance of the NOC-K. Besides this, O- and N-based functional groups render good wettability of the NOC-K, which can be visually confirmed by the small contact angle (~28°) (Fig. S5, see Supporting Information). It would promote deep wetting by aqueous electrolyte into the NOC-K sheets and make even larger inner surface ion accessible for efficient energy storage.

Electrochemical performance

Thanks to large SSA, moderate pore volume/size, and rich heteroatoms, the as-prepared NOC-K would be highly

Fig. 4 Fitted high-resolution XPS spectra of the hierarchical NOC-K. **a** Survey spectrum, **b** C 1s, **c** N 1s, and **d** O 1s
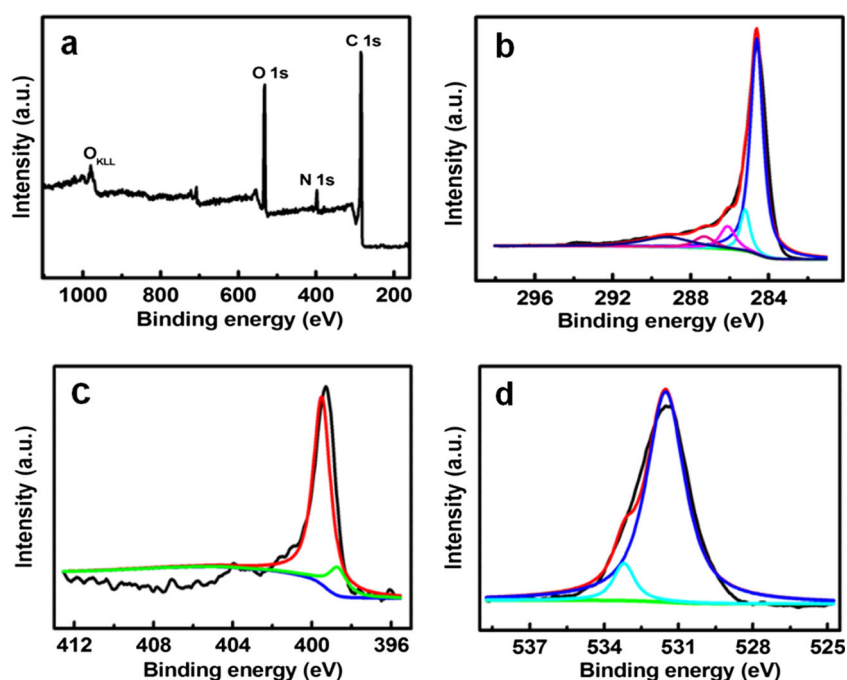
anticipated to perform as excellent electrode for ECs. The electrochemical performance of the NOC-K was firstly measured in three-electrode configuration with 6 M KOH as electrolyte. As presented in Fig. 5, CV curves of the NOC-K and NOC-Z, compared to the NOC electrode, exhibit a typical electric double-layer capacitive behavior with near rectangular shape with respect to the zero current line between −1.0 and 0.0 V (vs. SCE) at scanning rates of 5 (Fig. 5a) and 50 mV s^{-1} (Fig. 5b). Of note, the NOC-K demonstrates the largest electrochemical currents and integrated areas under the current-potential curve at the same rates, as seen in Fig. 5, indicating the highest charge storage capacity of the NOC-K even at a high rate of 50 mV s^{-1}. Furthermore, more rapid current response of the NOC-K on voltage reversal at each end potential, that is, a less sensible increase in iR drop (i.e., the slope of V/I on voltage reversal at each end potential) with the scanning direction of CV changing, is obviously observed. This finding strongly reveals the rapid charge propagation nature of the NOC-K in KOH electrolyte, which also can be verified by noticeable "box-like" shape (Fig. 6a) even with the scan rate up to 100 mV s^{-1}. The outstanding electrochemical behaviors of the NOC-K in 6 M KOH should be reasonably ascribed to its desirable electronic conductivity (~0.67 ohm) and small charge transfer resistance (~0.53 ohm), when compared to those for NOC and NOC-Z, as evaluated from the EIS data (Fig. S6, see Supporting Information), besides its large SSA and appealing pore structure (Table S2, see Supporting Information).

Galvanostatic CP tests over a large current range from 0.5 to 10 A g^{-1} were further conducted to evaluate potential application of the NOC-K as an appealing electrode for ECs. Figure 6b shows the typical CP plots within the potential window from −1.0 to 0.0 V (vs. SCE) at various current rates as indicated. The linear characteristics of the charge/discharge curves prove the representative double-layer capacitive nature of the NOC-K in 6 M KOH again. The gravimetric SCs of the NOC-K can be calculated from these CP plots (Fig. 6b), and typical SCs as a function of discharge current density are collected in Fig. 6c. Clearly, the mass SCs of the NOC-K are estimated as ~216, ~179, ~165, ~150, and ~136 F g^{-1} at current densities of 0.5, 1.0, 2.0, 5.0, and 10 A g^{-1},

respectively, higher than those of coal liquefaction residue (~125 F g^{-1}) and other coals (~170 F g^{-1}) [43]. By contrast, the NOC-Z delivers smaller SCs of ~162 and ~90 F g^{-1} at current rates of 1.0 and 10 A g^{-1}, respectively. It is also worthy of noting that the NOC just yields a SC of ~26 F g^{-1} at 0.5 A g^{-1}, and even 4 F g^{-1} at a high rate of 5 A g^{-1}. In view of charge storage mechanism and corresponding SCs of the three in KOH, we speculate the effective SSA order of the three as follows: NOC-K > NOC-Z > NOC. The largest electroactive SSA and suitable pore size of the NOC-K can be well responsible for its promising electrochemical capacitance observed in 6 M KOH.

One thing still cannot be ignored that the pseudo-capacitive effects arise from the heteroatoms of N and O in acidic electrolyte, as presented in Fig. 7. CV evaluation of the NOC-K was nextly carried out to further study the striking contribution of high-content pyrrolic/pyridonic N and quinine-type O groups to the overall electrochemical behaviors of the NOC-K in 1 M H$_2$SO$_4$. Figure 7a demonstrates the representative CV curves from 0.0 to 1.0 V (vs. SCE) of the NOC-K in 1 M H$_2$SO$_4$. Impressively, the electrochemical current subsequently increases while the CV shape almost keeps the same with the scan rates increasing, as demonstrated in the multi-scan rate voltammograms (Fig. 7a), suggesting good electrochemical capacitance of the unique NOC-K over the entire scan range from 5 to 100 mV s^{-1}. One should especially note that the E-I responses also feature extra appearance of prominent broad and overlapped humps ranged from ~0.3 to ~0.7 V (vs. SCE) with various sweep rates, which should originate from the combination of EDLC and Faradaic pseudo-capacitance related to the heteroatom functionalities of the NOC-K in 1 M H$_2$SO$_4$, rather than just the single EDLC (Figs. 5 and 6a). Therefore, the NOC-K yields even larger electrochemical currents, compared to those in KOH electrolyte (Figs. 5 and 6a), revealing the enhanced capacitance of the NOC-K in 1 M H$_2$SO$_4$. As evident in Fig. 7b, both of the electrochemically cathodic and anodic peak currents vary linearly with higher sweep rates, such as 50, 80, and 100 mV s^{-1}, demonstrating the excellent rate behavior of the NOC-K, although the Faradaic reactions are involved in the electrochemical process in H$_2$SO$_4$. Figure 7c further depicts the peak currents of the

Fig. 5 CV curves (**a**, 5 mV s^{-1}; **b**, 50 mV s^{-1}) of the NOC, NOC-Z, and NOC-K electrodes in 6 M KOH
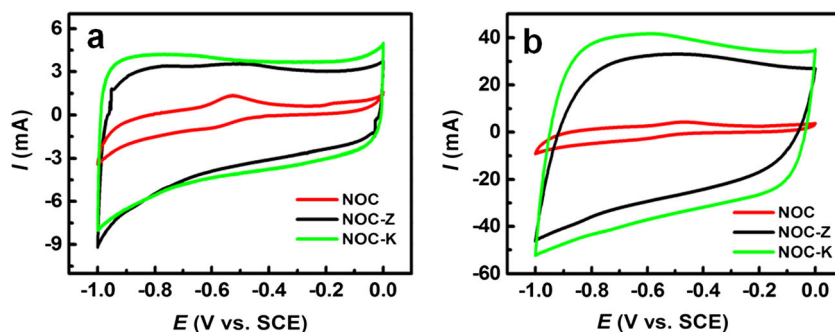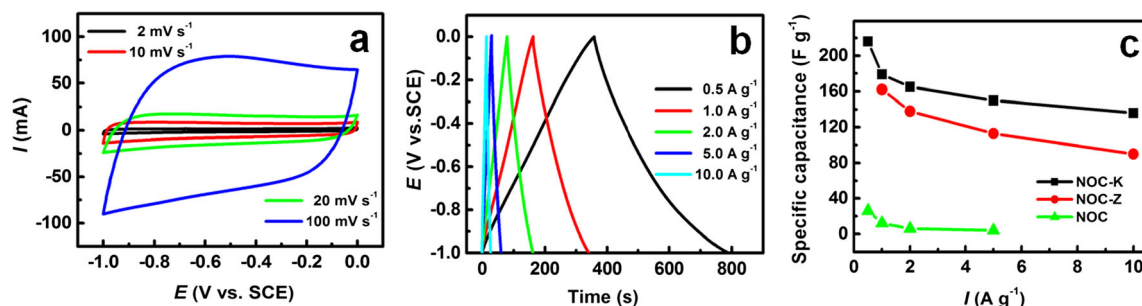
Fig. 6 CV curves at various sweep rates (**a**), CP plots (**b**), and calculated SC as a function of current density (**c**) of the as-prepared NOC-K electrode in 6 M KOH solution

NOC-K as a function of the square root of scan rate ($v^{1/2}$). The linear relationship of I vs. $v^{1/2}$ observed here shows a unique diffusion control process of the NOC-K electrode at lower scanning rates, such as 5, 10, and 20 mV s^{-1} [44–46]. Figure 7d demonstrates the typical charging/discharging plots of the NOC-K within the potential window from 0.0 to 1.0 V (vs. SCE) with a large current span from 0.2 to 10 A g^{-1}. Nonlinear charge/discharge curves are apparently presented, which should result from electrochemical adsorption/desorption and redox reactions at the electrode/electrolyte interface in 1 M H$_2$SO$_4$. And much larger SCs of 449, 291, 244, 208, 166, and 146 F g^{-1} can be calculated, based on the CP data in Fig. 7d, at current densities of 0.2, 0.5, 1.0, 2.0, 5.0, and 10 A g^{-1}, respectively, in 1 M H$_2$SO$_4$ (Fig. 7e), much higher than those in 6 M KOH (Fig. 6c). Considering the dimensional order of OH$^-$ < K$^+$ ≈ H$_3$O$^+$ (3.62–4.2 Å) < SO$_4^{2-}$ (5.33 Å) [47, 48], the double-layer capacitance contribution of electro-adsorption to the overall capacitance in 6 M KOH should be more pronounced than that in 1 M

H$_2$SO$_4$. However, the overall SC observed in 6 M KOH is even smaller than those in 1 M H$_2$SO$_4$. This leads us to believe the existence of extra contribution from the resultant pseudo-capacitance once more. More strikingly, the surface area-normalized capacitance of the NOC-K, considering its SSA, is reckoned as ~35.7 μF cm^{-2} at a current density of 0.2 A g^{-1} in 1 M H$_2$SO$_4$, much higher than the theoretical EDLC capacitance of the carbonaceous materials (10–25 μF cm^{-2}) [4, 44], verifying its high electrochemical surface utilization in aqueous acidic electrolytes. This should be reasonably attributed to a more sensitive effect of the basic oxygenated and nitrogenated surface functional groups of the NOC-K with enhanced wettability and proper porous feature in 1 M H$_2$SO$_4$, which gives rise to extra pseudo-capacitive effects from sufficient Faradaic redox reactions in acidic medium. Thus, we take it as proof-of-principle for the importance of structurally incorporated N and O species in the enhancement of the capacitive performance in 1 M H$_2$SO$_4$. Retention of the SC during continuous charge/discharge cycles at high rate
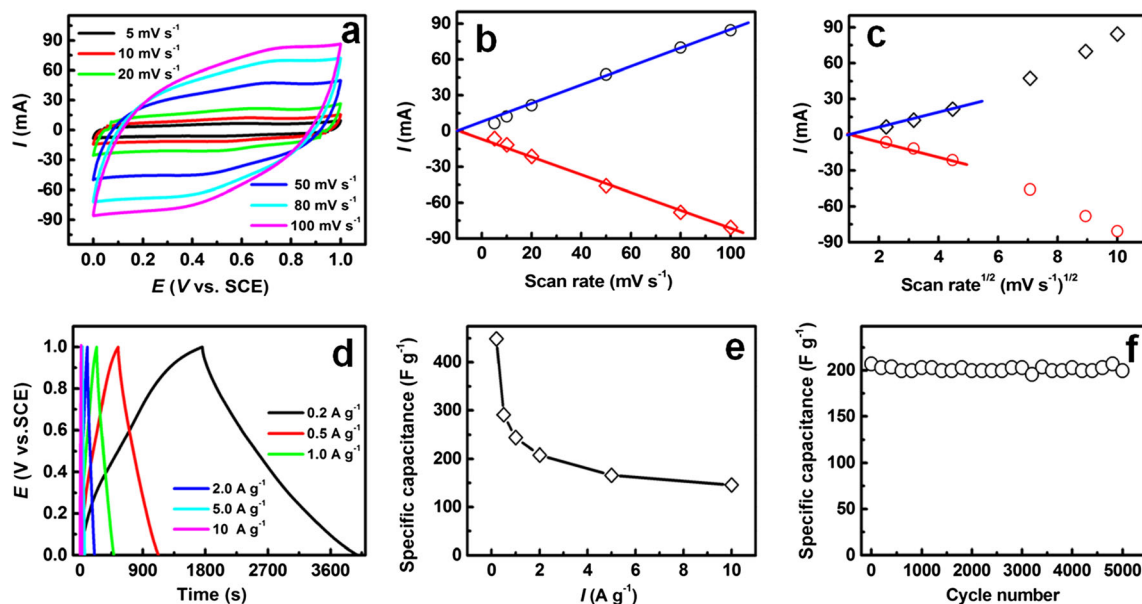

Fig. 7 CV curves at various sweep rates (**a**), the relationship between anodic and cathodic peak current and the sweep rate (**b**, 0.5 V), the current vs. $v^{1/2}$ (**c**, 0.5 V), CP plots (**d**), calculated SC as a function of

current density (**e**), and cycling performance (**f**, 2 A g^{-1}) of the as-prepared NOC-K electrode in 1 M H$_2$SO$_4$

operating condition is essential for practical viability of ECs. Figure 7f displays the long-term cycling performance of the NOC-K investigated by using CP measurement at large current rate of 2.0 A g^{-1} within a potential window of 0.0–1.0 V. Obviously, ~97 % of the initial SC is still maintained over 5000 continuous cycles, displaying excellent electrochemical stability of the NOC-K in 1 M H$_2$SO$_4$. The appealing electrochemical performance observed here could be reasonably attributed to the following characteristics. Firstly, large SSA of the NOC-K affords rich electrode/electrolyte sur-/interfaces for efficient charge accommodation. Secondly, the presence of O and N heteroatoms in NOC-K framework not only enhances its surface wettability to ensure a sufficient utilization of the exposed surface for effective charge storage but also produces stable pseudo-capacitance through Faradaic charge transfer reactions. Thirdly, the optimized PSD decreases the inner-pore ion-transport resistance and the diffusion distance in the NOC-K sheets. And finally, good electronic conductivity leads to a lower electron transport resistance on the NOC-K electrode, due to the typical nitrogen functionality, particularly the richness in bulk N for the NOC-K product [12, 49–51].

Further electrochemical investigation was carried out in 6 M KOH or 1 M H$_2$SO$_4$ by using symmetric devices with two identical electrodes constituted from the NOC-K within an electrochemical voltage window of 1.0 V. As evident in Fig. 8a, b, the NOC-K-based symmetric cells present quasi-rectangular CV shape at wide scanning rate spanning from 5 to 100 mV s^{-1}, which suggests the excellent electrochemical capacitance of the symmetric ECs both in aqueous H$_2$SO$_4$ and KOH electrolytes. Also note that the higher electrochemical current and larger integrated area under the *I-E* curve are observed for the symmetric device with 1 M H$_2$SO$_4$ (Fig. 8b), compared to those in KOH (Fig. 8a), revealing superior charge storage ability of the EC in 1 M H$_2$SO$_4$, owing to intriguing pseudo-capacitive attribution in such system. Based on typical CP plots (Fig. 8c, d) at various current densities ranged from 0.5 to 5 A g^{-1}, the SCs of the NOC-K-based symmetric EC can be calculated and summarized in Fig. 8e. Obviously, the symmetric device delivers a high SC of ~49 F g^{-1} at 0.25 A g^{-1}, and even ~19 F g^{-1} at a large current loading of 5 A g^{-1} in 1 M H$_2$SO$_4$, much higher than those (24 and 10 F g^{-1} at 0.25 and 5 A g^{-1}, respectively) in 6 M KOH at

Fig. 8 CV curves at various sweep rates (**a**, 6 M KOH; **b**, 1 M H$_2$SO$_4$), CP plots (**c**, 6 M KOH; **d**, 1 M H$_2$SO$_4$), calculated SC as a function of current density (**e**), and Ragone plots (**f**) of the symmetric ECs based on the hierarchical porous NOC-K electrode with different electrolytes as indicated
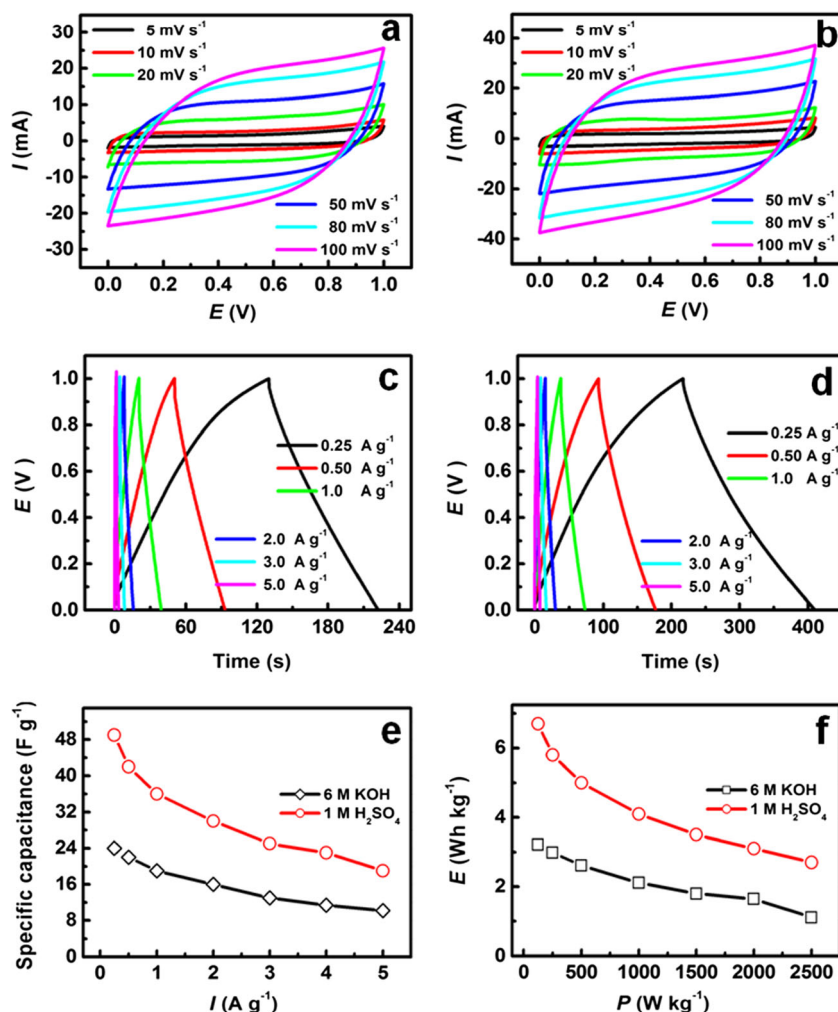
the same rates. Ragone plots for the symmetric devices with 1 M H_2SO_4 and 6 M KOH are further depicted in Fig. 8f. The symmetric device delivers a high SED of ~6.7 Wh kg^{-1} at a SPD of 125 W kg^{-1} in 1 M H_2SO_4, higher than those in 6 M KOH electrolyte. All in all, the electrochemical data mentioned above strongly confirms even better electrochemical capacitance of the NOC-K-based symmetric device in acidic electrolyte.

Conclusions

Inspired by the prospect of using the naturally abundant yet cost-efficient lignite in producing more high value-added mesoporous NOC towards advanced ECs, we carried out a thorough investigation on the influence of chemical activating agents upon morphology, pore structure, and electrochemical capacitance of the final products. Physicochemical and electrochemical characterizations illustrated that the NOC-K sheets were endowed with high SSA, large pore volume, and optimal pore size and delivered much better electrochemical performance than those for NOC and NOC-Z in 6 M KOH. Furthermore, benefiting from the appealing mesoporosity, large effective SSA, and Faradaic contribution from heteroatom doping effect, the NOC-K electrode obtained a large SC of 449 F g^{-1} at 0.2 A g^{-1} and excellent SC retention of ~97 % over 5000 continuous cycles in 1 M H_2SO_4. The NOC-K-based symmetric EC is fabricated with higher SED of ~6.7 Wh kg^{-1} in 1 M H_2SO_4. More significantly, our success in the evolution of NOC-based materials not only opened up the great possibility of preparing sustainable and cost-efficient materials for next-generation ECs but also constructed an economical platform for efficiently preparing high-performance NOC available for a large spectrum of applications.

References

1. Chmiola J, Yushin G, Gogotsi Y, Portet C, Simon P, Taberna PL (2006) Science 313:1760–1763
2. Zhang YZ, Wang Y, Cheng T, Lai WY, Pang H, Huang W (2015) Chem Soc Rev 44:5181–5199
3. Conway BE (1999) Electrochemical supercapacitors: scientific fundamentals and technological applications (Kluwer).
4. Li HQ, Luo JY, Zhou XF, Yu CZ, Xia YY (2007) J Electrochem Soc 154:A731–A376
5. Simon P, Gogotsi Y (2008) Nat Mater 7:845–854
6. Lee SW, Gallant BM, Byon HR, Hammond PT, Yang SH (2011) Energy Environ Sci 4:1972–1985
7. Guo BK, Sun XG, Veith GM, Bi ZH, Mahurin SM, Liao C, Bridges C, Paranthaman MP, Dai S (2013) Adv Energy Mater 3:708–712
8. Hou LR, Lian L, Li DK, Pang G, Li JF, Zhang XG, Xiong SL, Yuan CZ (2013) Carbon 64:141–149
9. Xu B, Hou S, Cao GP, Wu F, Yang YS (2012) J Mater Chem 22:19088–19093
10. Su FB, Poh CK, Chen JS, Xu GW, Wang D, Li Q, Lin JY, Lou XW (2011) Energy Environ Sci 4:717–724
11. Hulicova-Jurcakova D, Seredych M, Lu GQ, Bandosz TJ (2009) Adv Funct Mater 19:438–447
12. Béguin F, Szostak K, Lota G, Frackowiak E (2005) Adv Mater 17:2380–2384
13. Qian WJ, Sun FX, Xu YH, Qiu LH, Liu CH, Wang SD, Yan F (2014) Energy Environ Sci 7:379–386
14. Borchardt L, Oschatz M, Kaskel S (2014) Mater Horiz 1:157–168
15. Zhou HS, Li DL, Hibino M, Honma I (2005) Angew Chem Int Ed 117:807–812
16. Futaba DN, Hata K, Yamada T, Hiraoka T, Hayamizu Y, Kakudate Y, Tanaike O, Hatori H, Yumura M, Iijima S (2006) Nat Mater 5:987–994
17. Wei TY, Chen CH, Chien HC, Lu SY, Hu CC (2010) Adv Mater 22:347–351
18. Biswal M, Banerjee A, Deo M, Ogale S (2013) Energy Environ Sci 6:1249–1259
19. Huang WT, Zhang H, Huang YQ, Wang WK, Wei SC (2011) Carbon 49:838–843
20. Chen WX, Zhang H, Huang YQ, Wang WK (2010) J Mater Chem 20:4773–4775
21. Subramanian V, Luo C, Stephan AM, Nahm KS, Thomas S, Wei BQ (2007) J Phys Chem C 11:7527–7531
22. He XJ, Ling PH, Yu MX, Wang XT, Zhang XY, Zheng MD (2013) Electrochim Acta 105:635–641
23. Zhou L, Cao H, Zhu SQ, Hou LR, Yuan CZ (2015) Green Chem 17:2373–2382
24. Guo Y, Shi ZQ, Chen MM, Wang CY (2014) J Power Sources 252:235–243
25. Hulicova-Jurcakova D, Puziy AM, Poddubnaya OI, Suárez-García F, Tascón JMD, Lu GQ (2009) J Am Chem Soc 131:5026–5027
26. Ding M, Zhao YP, Zhu YY, Zong ZM, Wei XY, Fan X (2014) Energy Sources, Part A: Recovery, Utilization, and Environmental Effects 36:2027–2032
27. Doskočil L, Grasset L, Válková D, Pekař M (2014) Fuel 134:406–413
28. Yuan CZ, Chen L, Gao B, Su LH, Zhang XG (2009) J Mater Chem 19:246–252
29. Marsh H, Reinoso FR (2006) Activated carbon. Elsevier, Amsterdam
30. Raymundo-Piñero E, Azaïs P, Cacciaguerra D, Cazorla-Amorós D, Linares-Solano A, Béguin F (2006) Carbon 43:786–795
31. Wang JC, Kaskel S (2012) J Mater Chem 22:23710–23725
32. Świątkowski A (1999) In studies in surface science and catalysis. Ed. Dąbrowski, Elsevier, Vol. 120, Part A, P. 69.
33. Romanos J, Beckner M, Rash T, Firlej L, Kuchta B, Yu P, Suppes G, Wexler C, Pfeifer P (2012) Nanotechnology 23:015401
34. Caturla F, Molina-Sabio M, Rodríguez-Reinoso F (1991) Carbon 29:999–1007
35. Smisek M, Cerny S (1970) Active carbon: manufacture, properties and applications. Elsevier, Amsterdam
36. Yuan CZ, Gao B, Shen LF, Yang SD, Hao L, Lu XJ, Zhang F, Zhang LJ, Zhang XG (2011) Nanoscale 3:529–545
37. Zhou JH, Sui ZJ, Zhu J, Li P, Chen D, Dai YC, Yuan WK (2007) Carbon 45:785–796
38. Ma YW, Zhao J, Zhang LR, Zhao Y, Fan QL, Li XA (2011) Carbon 49:5292–5297
39. Wang ZH, Qie L, Yuan LX, Zhang WX, Hu XL, Huang YH (2013) Carbon 55:328–334

40. Li Z, Xu ZW, Wang HL, Ding J, Zahiri B, Holt CMB, Tan XH, Mitlin D (2014) Energy Environ Sci 7:1708–1718
41. Ania CO, Khomenko V, Raymundo-Pinero E, Parra JB, Béguin F (2007) Adv Funct Mater 17:1828–1836
42. Andreas HA, Conway BE (2006) Electrochim Acta 51:6510–6520
43. Zhang JB, Jin LJ, Cheng J, Hu HQ (2013) Carbon 55:221–232
44. Bard AJ, Faulkner LR (2001) Electrochemical methods fundamentals and applications, 2nd ed., John Wiley, Inc, New York; Ch. 6, P: 233–235.
45. Yuan CZ, Zhang LH, Hou LR, Lin JD, Pang G (2014) RSC Adv 4: 24773–24776
46. Pang H, Zhang YZ, Lai WY, Hu Z, Huang W (2015) Nano Energy 15:303–312
47. Eliad L, Salitra G, Soffer A, Aurbach D (2001) J Phys Chem B 105: 6880–6887
48. Ue M (1994) J Electrochem Soc 141:3336–3342
49. Paraknowitsch JP, Thomas A (2013) Energy Environ Sci 6: 2839–2855
50. Li WR, Chen DH, Li Z, Shi YF, Wan Y, Huang JJ, Yang JJ, Zhao DY, Jiang ZY (2007) Electrochem Commun 9:569–573
51. Yuan CZ, Zhou L, Zhu SQ, Cao H, Hou LR (2015) J Electrochem Soc 162:A781–A786